Salcedo-Abraira, P.; Babaryk, AA.; Montero-Lanzuela, E.; Contreras Almengor, OR.; Cabrero-Antonino, M.; Svensson, E.; Willhammar, T.... (2021). A Novel Porous Ti-Squarate as Efficient Photocatalyst in the Overall Water Splitting Reaction under Simulated Sunlight Irradiation. Advanced Materials. 33(52):1-9. https://doi.org/10.1002/adma.202106627

WILEY-VCH

A novel porous Ti-squarate as efficient photocatalyst in the overall water splitting reaction under simulated sunlight irradiation

Pablo Salcedo-Abraira,[1§] Artem A. Babaryk,[1§] Eva Montero-Lanzuela,[2§] Oscar R. Contreras-Almengor,[1] María Cabrero-Antonino,[2] Erik Svensson Grape,[3] Tom Willhammar,[3] Sergio Navalón,[2] Erik Elkäim,[4] Hermenegildo García,[2] Patricia Horcajada[1]

[§]*Equally contributing authors*

[1] Advanced Porous Materials Unit (APMU), IMDEA Energy, Avda. Ramón de la Sagra 3, 28935 Móstoles-Madrid, Spain
[2] Departamento de Química and Instituto de Tecnología Química (CSIC-UPV), Universitat Politècnica de València, Spain
[3] Department of Materials and Environmental Chemistry, Stockholm University, Stockholm, 106 91, Sweden
[4] CRISTAL Beamline, Synchrotron Soleil, L'orme des Merisiers, Saint-Aubin, BP 48, 91192 Gif-sur-Yvette Cedex, France

Keywords: Metal-Organic Framework, Titanium, Porosity, Water splitting photocatalysis

ABSTRACT:

A new porous titanium(IV) squarate metal-organic framework (MOF), denoted as IEF-11, having a never reported titanium secondary building unit -has been successfully synthesized and fully characterized. IEF-11 not only exhibits a permanent porosity, but also an outstanding chemical stability. Further, as a consequence of combining the photoactive Ti(IV) and the electroactive squarate, IEF-11 presents relevant optoelectronic properties, applied here to the photocatalytic overall water splitting reaction. Remarkably, IEF-11 as a photocatalyst is able to produce record H_2 amounts for MOF-based materials under simulated sunlight (up to 672 $\mu mol \cdot g_{catalyst}$ in 22 h) without any activity loss during at least 10 days.

1. Introduction

Despite the high potential of metal-organic frameworks (MOFs) [1–3] in various industrially relevant fields (*e.g.* separation, sensing, energy, biomedicine and catalysis, among others),[4–6] one of their major limitations is their poor hydrolytic stability.[7] MOF robustness strongly depends on the strength of the M^{n+}-ligand bond, generally increasing with the metal valence.

[8,9] The use of Group 4 element cations such as Zr^{IV} and Ti^{IV}, known by their high oxyphilicity,[10] has recently emerged as a general strategy to form robust MOFs. In this sense, although the number of Zr-MOFs has exponentially increased in the last years,[11] the number of reported Ti-MOF structures are still scarce (< 30, to the best of our knowledge).[12,13] This is probably explained by: i) the high Ti^{4+} oxophylicity, preferentially stabilizing titania rather than incompletely hydrolyzed titanium(IV) oxoclusters;[14] and ii) the high charge of Ti^{4+} that additionally complicates the synthesis of hybrid materials since higher valence cations involve a stronger competition between the inorganic polymerization and the formation of metal–ligand complexes.[15]

Apart from their *a priori* robustness, the growing interest of the scientific community in Ti-MOFs is also based on its economic and non-toxic character as well as on their relevant optoelectronic properties, associated to the d^0 electronic configuration of Ti^{4+} and to the photoinduced ligand-to-metal charge transfer of Ti←O bonds, also found in TiO_2.[16–21] As photocatalysts, Ti-MOFs demonstrate clear advantages compared with traditional titania: (i) selectivity control as a function of the porosity and composition;[22] (ii) tunability of their light absorption properties by the modification of the organic linker[23] and (iii) larger surface area and accessibility to the charge carrier traps.

In this work, we report the synthesis and full characterization of a new robust porous MOF (denoted as IEF-11; IEF stands for IMDEA Energy Framework), based on the photo- and redox-active Ti^{4+} and the electroactive squarate ligand (3,4-dihydroxycyclobut-3-ene-1,2-dionate, $C_4O_4^{2-}$). Structural elucidation of the nanoscaled IEF-11 crystals was made possible through the non-conventional three-dimensional electron diffraction (3DED) technique.[24] Remarkably, IEF-11 consists of an unusual secondary building unit (SBU), never reported so far, based on layers of interconnected TiO_5 and TiO_6 polyhedra. Further, IEF-11 shows a combined photo- and electro-activity derived from its Ti-metal nodes and squarate linkers,

making IEF-11 an excellent candidate for photocatalysis. Note here that, while other squarate-based MOFs exist, none of them have been proposed as photocatalysts.[25–30]

In this sense, among the most socioeconomically interesting photocatalytic reactions, overall water splitting using sun radiation is one of the most promising processes to generate green hydrogen. [31] In contrast with the hydrogen evolution reaction (HER; needing a sacrificial electron donor, as methanol or triethanolamine), overall water splitting takes place with only H_2O, with the HER and the oxygen evolution reaction (OER) occurring simultaneously. However, this reaction requires a very efficient photocatalyst due to the energetic requirement of the reaction and the complex O_2 formation mechanism that involves four electrons and four protons. Thus, while there are numerous reports employing MOFs (frequently associated to noble metal co-catalysts) as photocatalysts in HER,[32] only six MOFs have been reported so far as photocatalysts for overall water splitting.[16,33–38] Further, from these six, only three did not contain a co-catalyst, and all of them showed a similar photocatalytic performance. Even more challenging is the use of simulated sunlight instead of UV-Vis light, as MOFs tend to have limited absorption in the visible range. Considering the three examples mentioned before[34,36,37], these were the only materials that showed good performance under simulated sunlight and in the absence of a co-catalyst.

In this context, the present work describes the photocatalytic activity for both H_2 generation and overall water splitting under simulated sunlight irradiation of the nanosized Ti-squarate IEF-11. This solid exhibits the highest performance for overall water splitting using sunlight irradiation of any of the MOFs reported so far, with H_2 evolution rates from pure water at one sun illumination being more than 3 times higher than previously reported values. In addition, IEF-11 shows a remarkable photostability under long irradiation times. All in all, these results open a way to design efficient photocatalytic hybrid materials.

2. Results and discussion

2.1. Synthesis and characterization of IEF-11

A novel titanium(IV) squarate MOF (IEF-11) was solvothermally prepared (see experimental section for further details) after the optimization of the synthetic conditions (*i.e.* reaction time, temperature, concentration and nature of Ti precursor) using an efficient high-throughput method.[39] Briefly, high yields of pure IEF-11 (80 wt %) were obtained by heating a mixture of squaric acid (H_2SQ) and titanium butoxide in a mixture of glacial acetic acid and isopropanol at 120 ºC for 72 h. Notably, the synthesis was successfully scaled-up from a 2.5 mL- to 103 mL-reactor, obtaining 1.3 g of solid in a single reaction batch. In all cases, small well-faceted nanometric crystals with hexagonal geometry were isolated (85 ± 30 nm, n = 100; Figure 1), precluding structure unveiling by conventional single crystal X-ray diffraction. Consequently, the crystalline structure of IEF-11 was determined with the help of non-conventional three-dimensional electron diffraction (3DED) measurements using a *ca*. 100 nm single crystal (Table S1 and Figure S1 and S2) and by Rietveld refinements using high resolution synchrotron radiation powder X-ray diffraction patterns (SRPXRD; experimental section, Table S2 and Figure S3). IEF-11 [$Ti_2O_3(C_4O_4)$] (MW = 255.77 g·mol^{-1}) crystallizes in the hexagonal space group *P*6/*mmm* (a = 10.5206(9) Å and c = 7.1903(6) Å). Ti2 (2*d* site, Wyckoff notation hereinafter) is located at the 3-fold axis and surrounded by three O2 atoms at 1.82 Å in the equatorial plane and apically distant from two O3 at 2.01 Å. Interestingly, the coordination geometry of Ti2 is that of a trigonal bipyramid (D_{3h}), something which has previously not been observed in titanium coordination polymers. Each O2 donor atom is shared with neighbor Ti1 (6*k*) [*d*(Ti1-O2 = 2.08 Å). The coordination sphere of the latter is completed by pairs of O4 and O1 atoms, with bond distances of 2.00 and 1.81 Å, respectively. Integrally, $Ti1O_6$ adopts a distorted octahedral configuration due to the well-known second Jahn-Teller effect[40] (Figure S4).~~[40]~~ Two $Ti1O_6$ octahedra are linked across common O2–O2^i (*i*: −*x*, 1−*y*, *z*) edge into Ti_2O_{10} bioctahedra. The latter shares a common O2 vertex with two adjacent moities at π/3, forming an equilateral triangle enclosing a TiO_5 located in its center

of gravity (Figure 2). This assembly of one TiO_5 and three Ti_2O_{10} polyhedra in the *ab*-plane may be considered as the SBU, connected infinitely into 2D layers and interlinked by disordered squarate anions along the *c* axis (Figure 2). Interestingly, the squarate residues do no adopt local regular geometry and are statically disordered, having two distinct modes of coordination. In the first mode a single squarate anion will be shared between two Ti2 cations and two of the 12 equivalent ~~neighbouring~~neighboring Ti1 cations that are equally likely to form a connection, as they are all within an appropriate distance. This gives an occupancy of said squarate of 1/6. The second mode consists of a squarate anion joining edge-sharing Ti1 cations. Since the direction of the first coordination mode would hinder the second mode of coordination 1/3 of the time, the occupancy for the second squarate anion is 2/3. As such, the arrangement of adjacent squarate anions would propagate throughout the structure, yet be statically disordered due to the equivalence of the possible arrangements, the coordination still allows for a complete coordination of Ti cations. Each linker either coordinate to four Ti1 or to two Ti1 and two Ti2. The metal-oxide layers are further stacked in an eclipsed way, leading to the formation of 1D hexagonal channels running along the *c* axis (diameter ~ 4.5 Å; considering Van der Waals radii). In order to confirm the accessibility of this potential 1D porosity, N_2 sorption experiments were carried out at 77 K (Figure ~~S4~~S5), obtaining a type I isotherm characteristic of microporous materials with a Brunauer-Emmett-Teller (BET) surface area and a micropore volume of 120 $m^2 \cdot g^{-1}$ and 0.06 $cm^3 \cdot g^{-1}$, respectively. The Horvath-Kawazoe (HK) pore size distribution (Figure S6) showed a maximum at around 5Å, in good agreement with the crystallographic data.

Con formato: Subrayado

Con formato: Subrayado, Sin Resaltar

Con formato: Sin Resaltar

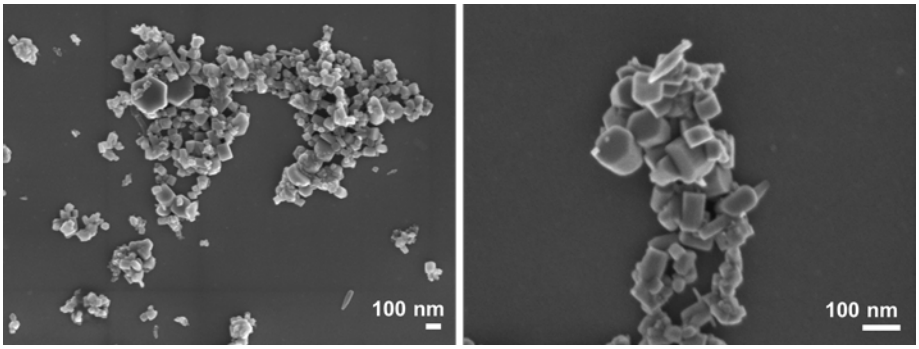

Figure 1: SEM images of IEF-11 at different magnifications.

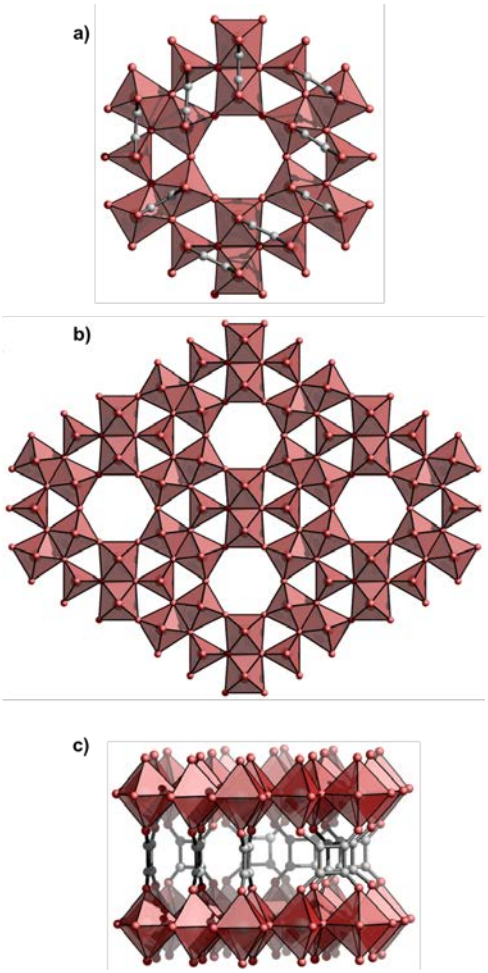

Figure 2: View along [001] of the IEF-11 structure (a), Ti-O layer SBU (b) and squarate linkers connecting the different Ti-O layers (c).

FTIR spectrum confirms the presence of coordinated SQ by a characteristic band at 1500 cm^{-1} that corresponds to the ν(CO), while the band at 1650 cm^{-1} coming from the free linker is not observed (Figure ~~S5~~S7). Upon heating (200 ºC), physisorbed water molecules (3200 cm^{-1}) and acetate moieties (coming from the solvent, 1700 cm^{-1}) were removed from the outer surface of the material, (Figure ~~S6~~S8). In agreement to the crystal structure, the chemical formula of the

IEF-11 [Ti_2O_3-(C_4O_4)] was confirmed by elemental analysis (C) and ICP-OES (Ti), being the oxygen estimated by difference (Theo. wt %: C – 18.8; Ti – 37.4; O – 44.3. Exp. wt %: C – 19.5±0.08; Ti – 35.7±1.8; O – 44.3). Note here that IEF-11 was preheated at 200 ºC also to eliminate remaining acetate moieties located also on the external surface of the nanocrystals (exp. wt % before and after heating: C = 20.2; H = 0.6 and C = 19.5; H = 0; respectively). The higher amount of exp C when compared with the theoretical value could be attributed to residual acetate moieties remaining in the material after heating at 200 ºC. XPS analysis of IEF-11 confirmed the expected composition and oxidation state of the elements present in the MOF (Figure ~~S7~~S9). In particular, C1s spectrum shows the characteristic signals of squarate ligand, characterized by sp^2 carbons (284.4 eV) together with C-O (286.1 eV) and C=O (288 eV). Note here that the high C=O energy value might correspond to some remaining acetate moieties from the synthesis, as previously mentioned. The O1s signals are mainly attributed to the presence of Ti-O bonds (529 eV) in the SBU of IEF-11, together with a broad band corresponding to C-O and C=O bonds belonging to the squarate. It should be noted that the broad bands of XPS C1s and O1s appearing at higher binding energy may also be partially attributed to the presence of acetic acid, employed as modulator during the synthesis of IEF-11, in agreement with the elemental analyses. The XPS Ti2p is attributable to the presence of Ti^{4+} ions in the SBU, as revealed by the $Ti2p^{3/2}$ (458 eV) and $Ti2p^{1/2}$ bands (463.7 eV).

In agreement to this, TGA curve shows two weight losses (Figure ~~S8~~S10). The first one (from RT to 200 ºC, 3.2 wt.%) can be attributed to the removal of water molecules physisorbed on the outer surface of the IEF-11 nanocrystals (in agreement with the FTIR spectroscopic data) and to the residual acetate (in agreement with XPS data and elemental analysis). The second weight loss, at around 300 ºC (42 wt.%), corresponds to the decomposition of the network by the oxidation and departure of the linker, leading to a final anatase TiO_2 residue, as identified by PXRD (ICSD-9852).[41] The thermal stability of IEF-11 was more precisely evaluated by VTPXRD (Figure ~~S9~~S11). IEF-11 preserves its structural integrity up to 300 ºC, in good

agreement with the TGA data. In addition, SEM images provided in Figure S# show that the morphology of the particles remains unaltered up to 250 ºC, showing a notable change in shape when the IEF-11 sample is heated at 300 ºC.

Con formato: Superíndice

Con formato: Superíndice

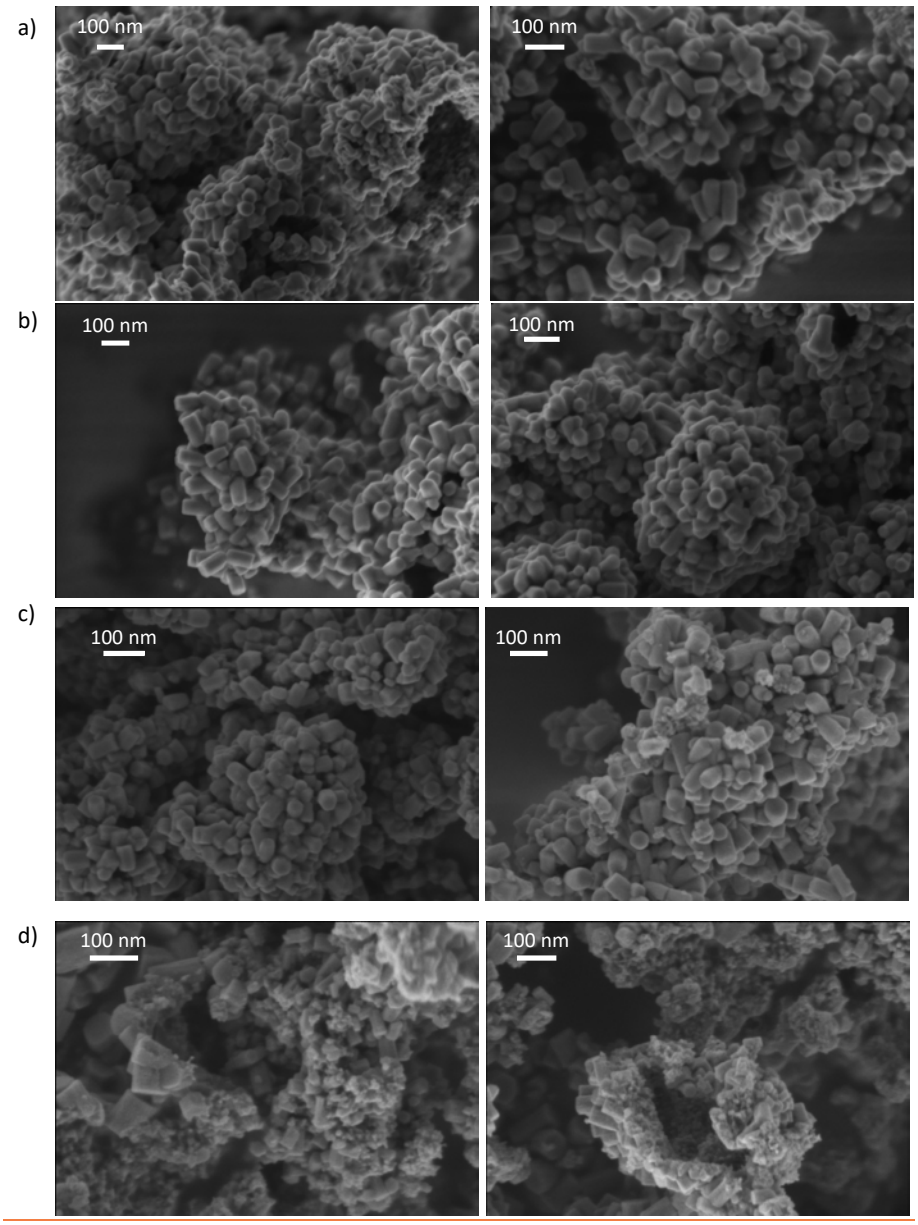

Figure S#. HR-SEM images of as-prepared IEF-11 sample (a) and IEF-11 sample calcined at 200 (b), 250 ºC (c) and 300 ºC (d).

The chemical robustness of the IEF-11 was assessed by suspending overnight the powdered material in a variety of organic solvents commonly used in catalysis, in aqueous solutions at different pH (from 1 to 12) and in water under UV-Vis irradiation (see experimental section in the ESI for further details). After the experiments, the structural integrity of IEF-11 in organic (hexane, dichloromethane-CH_2Cl_2, acetonitrile-AcN, N,N'-dimethylformamide-DMF, dimethyl sulfoxide-DMSO and isopropanol-^{i}PrOH) and aqueous conditions was confirmed by PXRD (Figure ~~S10~~ S12 and ~~S11~~S13). Further, its high chemical robustness was confirmed for a broad pH range (from 1 to 10.5), quantifying a maximum of 6 wt.% of the total linker leached after 16 h at pH = 10.5 (Figure ~~S11~~S13). Under more aggressive alkaline conditions (pH=12), PXRD pattern shows noticeable peak broadening consistent with partial degradation, which is associated with a ligand leaching of 30 wt.%. Remarkably, IEF-11 displays an exceptional stability in aqueous suspension under UV-vis irradiation, with only 2 wt.% of released ligand after 24 h (Figure ~~S12~~S14). Such outstanding structural stability and chemical robustness, together with an extension of the light absorption to the visible range (E_g = 2.45 eV; determined by diffuse reflectance UV-Vis spectroscopy, Figure ~~S13~~S15), make IEF-11 a promising candidate for photocatalysis.

The valence band energy maximum was estimated from XPS by determining the minimum energy to observe the appearance of electrons, resulting in a potential of 1.364 V *vs.* normal hydrogen electrode (NHE) after correction by the work function of the instrument (see supporting information for a detailed description of the calculations).[42] From this value, the conduction band energy minimum was deduced by adding the optical bandgap. Figure 3 illustrates the alignment of the valence and conduction band energy values with respect to the potential required for H_2 and O_2 generation from H_2O at pH 0.

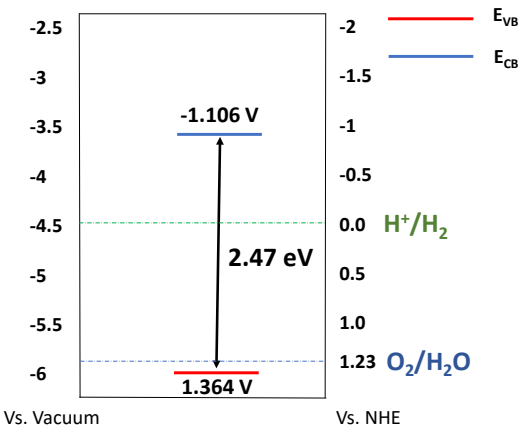

Figure 3: Energy band diagram of IEF-11 and thermodynamic potentials with respect to NHE for H_2 and O_2 evolution from H_2O.

2.3. Photocatalytic performance of IEF-11

Prior to performing liquid phase photocatalytic studies, the hydrodynamic diameter of the IEF-11 nanoparticles in H_2O and EtOH was assessed by dynamic light scattering (DLS), finding quite monodispersed small particles of sizes of 84±6 and 117±16 nm, respectively (Table S3; polydispersity index-PdI ~ 0.3). These values are in good agreement with the particle size estimated by SEM (85 ± 30 nm, Figure 1), indicating that IEF-11 crystals are well dispersed with no particle aggregation. The slightly smaller crystal dimensions in water when compared with ethanol could be justified by the smaller size of water solvation layer.[43] In addition, the negatively charged surface of the particles (-39 and -38 mV in water and ethanol, respectively) could be explained by the presence of squarate groups on the particle surface. This conclusion is further supported by the evaluation of the particle size and ζ-potential as a function of the pH (Figure ~~S14~~S16). At very low pH (pH = 1), particle agglomeration (1150 nm) is observed, probably related to an almost neutral ζ-potential (-7 mV) as a consequence of the protonation of the squarate groups (pK_{a1} = 1.5). At higher pH

(pH > pK_a), the squarate groups at the surface of the material will be deprotonated, providing a negative charge (around -40 mV) to the colloidal particles that results in enough electrostatic repulsions (typically found for ζ-potential values higher than + / - 30 mV) [44] and then, a persistent dispersion. Even more, the nanometric size of the IEF-11 crystals presents an important external surface area (estimated from the *t*-plot method = 40 $m^2 \cdot g^{-1}$; Figure ~~S5~~S5), which might be beneficial for heterogeneous catalysis, increasing the number of available active sites interacting with both the light and the reagents.[45]

The photocatalytic experiments were initially carried out under both UV-Vis and simulated sunlight from a Hg-Xe lamp (150 W) through an AM 1.5G filter without cooling system (35 ºC). To optimize the photocatalyst concentration, IEF-11 was first suspended in MilliQ water (20 mL) at an initial pH=6 at four different concentrations. Although evolution of H_2 and O_2 was observed in all cases, a non-linear relationship between H_2 production and photocatalyst mass was evidenced (Table 1). Observation of an optimal IEF-11 concentration to achieve~~e~~ the highest H_2 evolution rate is assumed to derive from the balance between: i) the positive influence of the higher concentration on the light harvesting and ii) the negative influence of an increasing turbidity and lack of light penetration inside the photoreactor when the photocatalyst concentration increases. An optimal concentration of 0.125 $mg \cdot mL^{-1}$ was determined for the highest H_2 production. The following experiments, however, were performed using 0.25 $mg \cdot mL^{-1}$ that in addition of a close to optimal H_2 evolution allows characterization of the catalyst after its use by PXRD. The influence of the temperature was determined by performing two additional experiments at 5 and 10 ºC using a cooling system. As it can be seen in Table 1, decreasing the temperature results in an activity diminution, while still achieving a remarkable photocatalytic activity even at 5 ºC.

Table 1: Photocatalytic overall water splitting into H_2 and O_2 using IEF-11 under different reaction conditions.

Temperature (°C)	Amount of catalyst (mg)	Simulated sunlight ($\mu mol \cdot g_{cat}^{-1}$ H_2 / O_2)		UV-Vis. light ($\mu mol \cdot g_{cat}^{-1}$ H_2 / O_2)	
		5 h	22 h	5 h	22 h
35	20	75 / 32	185 / 78	88 / 34	224 / 98
	10	150 / 59	260 / 107	160 / 61	340 / 143
	5	220 / 103	540 / 267	235 / 102	610 / 262
	2.5	250 / 112	672 / 322	290 / 140	765 / 295
10	5	94 / 53	276 / 112	179 / 77	563 / 211
5	5	63 / 24	158 / 68	98 / 36	220 / 87

The high H_2 production in the overall water splitting measured for IEF-11 as solar photocatalyst deserves a comment. Although comparison with literature values needs always to be taken

~~**Table 1**: Photocatalytic overall water splitting using IEF-11 under different reaction conditions.~~

~~Temperature (°C)~~	~~Amount of catalyst (mg)~~	~~Simulated sunlight ($\mu mol \cdot g_{cat}^{-1}$)~~		~~UV-Vis. light ($\mu mol \cdot g_{cat}^{-1}$)~~	
		~~5 h~~	~~22 h~~	~~5 h~~	~~22 h~~
~~35~~	~~20~~	~~75~~	~~185~~	~~88~~	~~224~~
	~~10~~	~~150~~	~~260~~	~~160~~	~~340~~
	~~5~~	~~220~~	~~540~~	~~235~~	~~610~~
	~~2.5~~	~~250~~	~~672~~	~~290~~	~~765~~
~~10~~	~~5~~	~~94~~	~~276~~	~~179~~	~~563~~
~~5~~	~~5~~	~~63~~	~~158~~	~~98~~	~~220~~

cautiously due to the variability in light intensity, photoreactor design and operational conditions, among other parameters influencing H_2 evolution, data presented in Table S4 for

Con formato: Sin Resaltar

IEF-11 compare favorably with the highest H_2 production rates achieved so far using different MOFs or other semiconducting photocatalysts. Remarkably, the activity of IEF-11 is much higher than those previously reported using simulated sunlight, particularly considering that IEF-11 does not incorporate noble metals or O_2 evolution co-catalysts. Among the most active reported MOF-based photocatalysts, one should mention a complex Zn-porphyrin system that uses $[Ru(2,2\text{-pipyridine})_3]^{2+}$ centers as photosensitizers and Ir–bipyridine catalytic centers, encapsulated within the hydrophilic interior of a liposome and in the presence of two redox relays: Fe^{3+}/Fe^{2+} ions (in the aqueous phase) and tetrachlorobenzoquinone (TCBQ)/ /tetrachlorobenzohydrosemiquinone (TCBQH) pair (in the organic phase), exhibiting a production of 836 µmol g^{-1} in 72 h under LED light irradiation. [46] In comparison with this complex multicomponent system, IEF-11 exhibits higher performance in terms of production (672 µmol g^{-1} in 22 h *vs.* 836 µmol g^{-1} in 72 h from the liposome system) and high photocatalytic stability upon~~efficient~~ reuse~~s~~ (up to 10 days *vs.* unreported reuses). In addition, IEF-11 is a much simpler photocatalytic system constituted by a single material with lower cost (derived from the absence of expensive noble-metals as Ru or Ir that are present in the liposome system).

One can hypothesize that the high photocatalytic activity of IEF-11 is a consequence of: i) its narrow bandgap and increasing solar light harvesting due to squarate ligands (2.45 eV measured from the Tauc plot in Figure ~~S13~~S15); ii) an appropriate band energy alignment for H_2 and O_2 evolution; and iii) the structural arrangement of 2D Ti-O-Ti motifs in IEF-11, allowing efficient and fast charge separation.

One remarkable feature of IEF-11 photocatalyst is that its photoresponse arises largely from absorption in the visible light range. For comparison, Figure 4 shows the temporal profile of H_2 and O_2 evolution upon irradiation of IEF-11 with a Hg-Xe lamp, visible light or simulated sunlight irradiation. Thus, H_2 generation under simulated sunlight is comparable to the production using the full UV zone of the Hg-Xe lamp, while more than 48% of the H_2

production comes from the visible light irradiation (λ > 455 nm). This means that the H_2 generation activity of IEF-11 is mainly due to photons in the visible range, in accordance with its notably narrow bandgap. Further, the solar-to-hydrogen (STH) conversion achieved using IEF-11 (2.5 mg *per* 20 mL) during the photocatalytic overall water splitting operating at 35 ºC under UV-Vis or simulated sunlight irradiation was 0.0008 and 0.001 %, respectively, which is in the range of the best-performing MOFs.[34] Importantly, the generation of O_2 coming from H_2O was confirmed by performing an experiment using isotopically labelled $H_2{}^{18}O$, detecting the formation of isotopically labelled $^{18}O_2$ (Figure ~~S15~~S17).

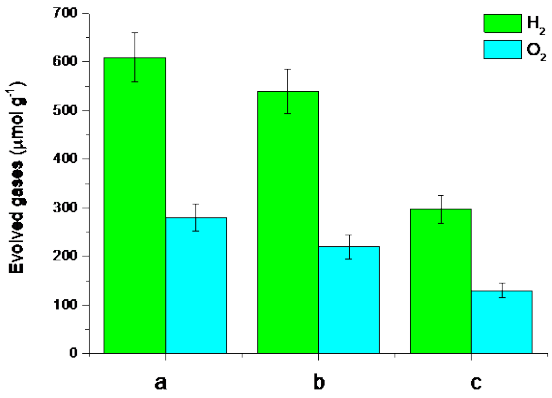

Figure 4: Photocatalytic overall water splitting using IEF-11 under UV-Vis (a), simulated sunlight (b) and visible light (λ > 455 nm) (c) irradiation. Reaction conditions: Photocatalyst (5 mg), H_2O (20 mL), 35 ºC, irradiation source (Hg-Xe lamp 150 W equipped or not with an AM 1.5G filter or 455 nm filter), reaction time 22 h.

With the aim to determine the relative rates of H_2 and O_2 evolution, photocatalytic experiments in the presence of sacrificial electron donors and acceptors were carried out. The addition of the electron donor methanol leads to a significant increase of the H_2 production by IEF-11 (*i.e.* from 210 to 1391 µmol $H_2 \cdot g^{-1}$ photocatalyst in 5 h under simulated sunlight).

Although the increase in the H_2 production by a factor of 3 is notable, it is much lower than those observed for other photocatalysts (*i.e.* typically over one order of magnitude).[16] An analogous experiment using Ce^{IV} as electron acceptor increases the O_2 evolution from 107 to about 1124 μmol $O_2 \cdot g^{-1}$ catalyst, also in 5 h. This increase on the O_2 production is higher than that of the H_2 generation, and would indicate that O_2 evolution is the slowest semireaction, as frequently observed since the formation of an O_2 molecule requires the removal of four electrons and four protons from two water molecules.

A well-known strategy to increase the H_2 evolution and the activity of photocatalysts is deposition of Pt nanoparticles.(Amarajothi Dhakshinamoorthy, Abdullah M. Asiri, Hermenegildo García Metal–Organic Framework (MOF) Compounds: Photocatalysts for Redox Reactions and Solar Fuel Production. Angew. Chem. Int. Ed. 55, 2016, 5414-5445~~ref~~) In the present case Pt nanoparticles were supported on IEF-11 by irradiation with a 300 W Xe lamp during 60 min an aqueous solution of H_2PtCl_6 containing EtOH as sacrificial electron donor to render Pt/IEF-11. Chemical analysis indicates that the Pt loading on Pt/IEF-11 is 1 wt.%. TEM images in dark field of Pt/IEF-11 show the presence of Pt nanoparticles smaller than 3 nm, with an average size about 1,6 nm (Figure S#). The Pt/IEF-11 solid was also employed as photocatalyst for the hydrogen evolution in the presence of methanol as sacrificial electron donor as well as for the overall water splitting under simulated sunlight irradiation. The results obtained show that the presence of Pt NPs supported on IEF-11 increases the photocatalytic activity for the hydrogen evolution reaction to 2540 μmol h^{-1} after 5 h compared to the pristine IEF-11 sample (1391 μmol $H_2 \cdot g^{-1}$) under simulated sunlight irradiation. In the case of the photocatalytic overall water splitting the use of Pt/IEF-11 sample as photocatalyst increases the production of both H_2 and O_2 (658 and 302 μmol g^{-1}) respect to the IEF-11 sample (540 and 267 μmol g^{-1}) under simulated sunlight irradiation after 22 h of reaction.

Con formato: Subíndice
Con formato: Sin Resaltar
Con formato: Subíndice
Con formato: Subíndice
Con formato: Sin Resaltar
Con formato: Fuente: Symbol
Con formato: Superíndice
Con formato: Fuente: Symbol
Con formato: Subíndice
Con formato: Superíndice
Con formato: Subíndice
Con formato: Subíndice
Con formato: Fuente: Symbol
Con formato: Fuente: Symbol

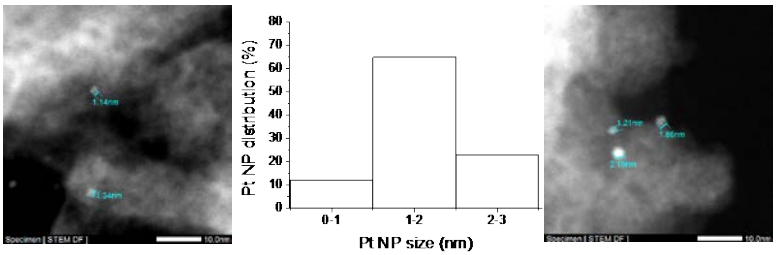

Figure S#. Representative TEM images and Pt NP distribution of Pt/IEF-11 solid. Note: the average Pt particle size is 1.61 nm.

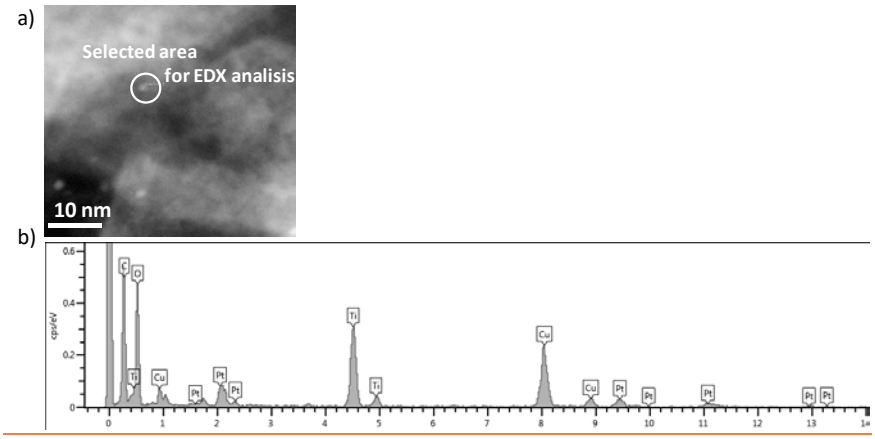

Figure #. Representative TEM image of Pt/IEF-11 solid and selected area (a) for EDX analisis (b). The presence of copper in the EDX spectrum due to the copper grid employed for the measurement.

From a practical point of view, the photocatalyst stability is one crucial issue to be considered. Precedents have shown that carboxylate ligands tend to undergo photodecarboxylation upon UV-light irradiation.[47] In the present case, IEF-11 remarkably exhibits a constant temporal H_2 and O_2 evolution profile upon ten consecutive reuses of 24 h each (Figure 5). The temporal profiles of H_2 and O_2 evolution show for each run a lack of linearity at longer times with lesser photocatalytic activity due to the accumulation of these gases in the photoreactor and their activity quenching holes (by H_2) and electrons (by O_2). Nevertheless, the temporal profiles of the reuses shown in Figure 5 were almost coincident. After 10 days irradiation, the

Con formato: Subíndice
Con formato: Subíndice
Con formato: Sin Resaltar
Con formato: Subíndice
Con formato: Subíndice
Con formato: Sin Resaltar
Con formato: Sin Resaltar

crystal structure of IEF-11 was maintained (as confirmed by PXRD; Figure 4), although a progressive leaching of the squarate ligand was detected by UV-Vis quantitative analysis in the mother liquors (*ca.* 0.6, 10.5 and 19.2% after 1, 7 and 10 days, respectively).

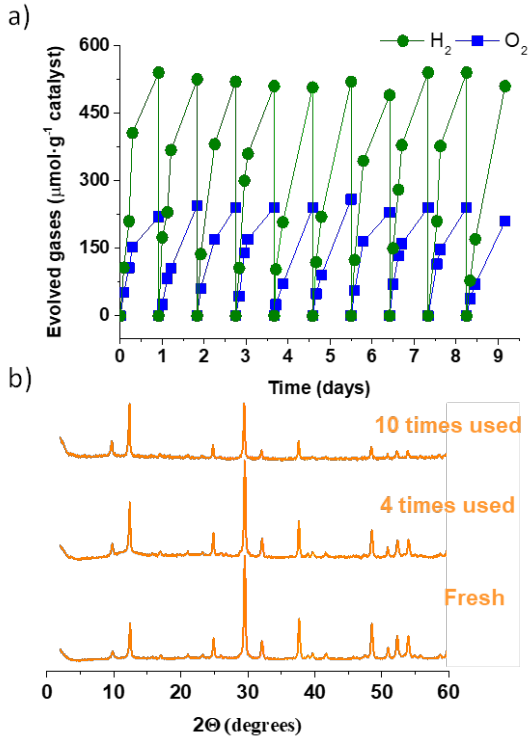

Figure 5: (a) Photocatalytic overall water splitting for ten consecutive cycles using IEF-11 under simulated sunlight irradiation and (b) PXRD patterns of the fresh, four- and ten-times used IEF-11 sample. Reaction conditions: photocatalyst (5 mg), H_2O (20 mL), simulated sunlight irradiation (Hg-Xe lamp 150 W through an AM 1.5G filter), 35 ºC.

The generation of the charge separated state upon irradiation was confirmed by using methyl viologen (MV) and *N,N,N',N'*-tetramethyl-*p*-phenylenediamine (PDA) as visual probes of the occurrence of photoinduced reduction and oxidation.[48] Both organic compounds generate relatively stable-colored radical cations, with characteristic UV-Vis absorption spectra, that

allow the visual and spectroscopic detection of the occurrence of the photocatalytic reaction. The results show that MV undergoes reduction to $MV^{+\cdot}$ radical cation by photogenerated electrons upon irradiation of IEF-11 in deuterated aqueous solution in the presence of methanol as electron donor, while PDA undergoes oxidation to $PDA^{+\cdot}$ radical cation by photogenerated holes upon irradiation of IEF-11 under argon atmosphere. Figure ~~S16~~ S18 shows a selection of the UV-Vis spectra as a function of the irradiation time of IEF-11 aqueous solution showing the growth of $MV^{+\cdot}$ and $PDA^{+\cdot}$ radical cations.

Photocurrent generation is also a convincing evidence of the occurrence of photoinduced charge separation.[49] Thus, photoelectrodes of IEF-11 were prepared by spreading a thin film of this material on transparent conductive fluorine-doped tin oxide (FTO). The photoelectrode was illuminated in contact with 0.1 M tetrabutylammonium hexafluorophosphate (TB_4PF_6) electrolyte using a Pt wire as counter electrode and Ag/AgCl as reference electrode in a single compartment cell (Figure ~~S17~~S19). It was observed that the anodic or cathodic current significantly increases in intensity by adding in the electrolyte solution methanol or $Ce(NO_3)_6(NH_4)_2$ as electron donor or acceptor, respectively. Thus, all the available data confirm that, upon illumination with visible light, IEF-11 undergoes excitation of the squarate ligand that transfers one electron to electron-deficient Ti^{IV}, leaving initially a radical cation on the squarate ligand and forming a Ti^{III} transient. Figure 6 summarizes the proposal. The occurrence of this charge separation with the generation of electrons on Ti nodes and holes on squarate ligands was supported by EPR spectroscopy. -In these measurements, irradiation of IEF-11 in acetonitrile containing TEOA allows recording an EPR signal attributable to Ti^{III} (Figure S19). Similar EPR measurements of IEF-11 irradiation in water and subsequent freezing at 77 K did not allow detecting any EPR signal. These results are in good agreement with previous report by Li and coworkers on a related Ti MOF MIL-125-NH_2. Yanghe Fu,Dengrong Sun,Yongjuan Chen,Renkun Huang,Dr. Zhengxin Ding,Prof. Dr. Xianzhi Fu,Prof. Dr. Zhaohui Li An Amine-Functionalized Titanium Metal–Organic Framework

Con formato: Sin Resaltar
Con formato: Superíndice
Con formato: Sin Resaltar
Con formato: Superíndice
Con formato: Sin Resaltar
Con formato: Sin Resaltar
Con formato: Sin Resaltar
Con formato: Sin Resaltar
Con formato: Sin Resaltar
Con formato: Superíndice
Con formato: Sin Resaltar
Con formato: Subíndice
Con formato: Sin Resaltar

Photocatalyst with Visible-Light-Induced Activity for CO2 Reduction. Angew. Chem. Int. Ed. 51, 2012, 3364-3367.

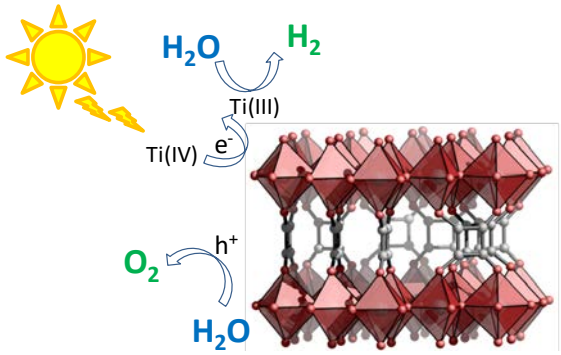

Figure 6. Mechanistic proposal of the photocatalytic overall water splitting on IEF-11 implying charge separation with electrons in Ti forming Ti^{III} and holes on the squarate ligand giving rise to H_2 and O_2, respectively.

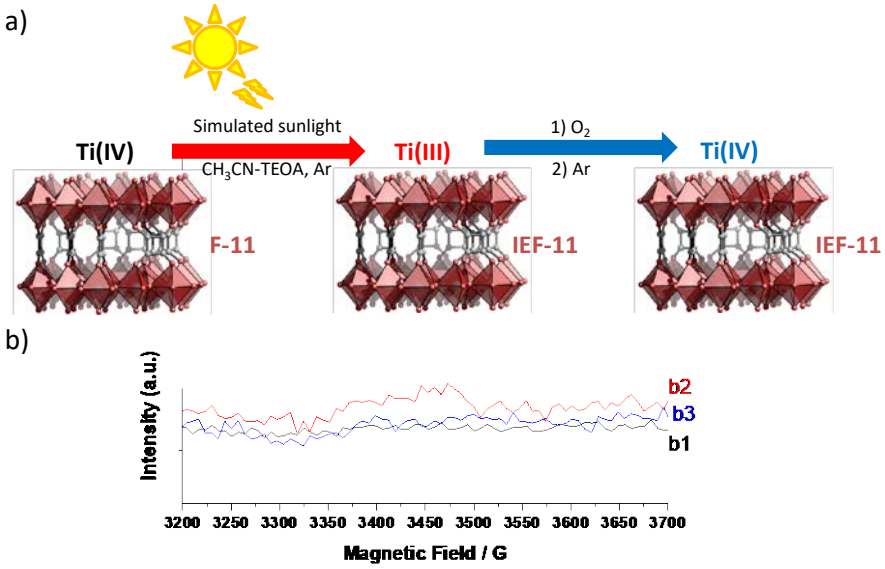

Figure S19. (a) Illustration of the changes occurred in the4 IEF-11 solid upon simulated sunlight irradiation via a photoinduced LMCT pathway. b) EPR spectra of IEF-11 in the dark (b1), IEF-11 under illumination (b2) or IEF under illumination after purging the sample with O2 and recorded under Ar (b3).

Con formato: Sin Resaltar
Con formato: Superíndice
Con formato: Subíndice
Con formato: Subíndice

3. Conclusion

A new highly robust and porous titanium(IV) squarate MOF (denoted as IEF-11) has been solvothermally synthesized and fully characterized. Due to the relevant visible optical absorbance of squarate dye and the original SBU based on 2D layers of interconnected TiO_5 and TiO_6 polyhedra, IEF-11 possesses a suitable bandgap and band alignment to efficiently perform overall water splitting photocatalysis. Without further modification, IEF-11 is able to produce H_2 and O_2 at rates among the highest ever reported, a significant portion of the photoresponse (~50 %) arising from the visible range. Further, the IEF-11 photocatalyst remains stable for extended irradiation periods (10 days) without any significant loss of crystallinity and photocatalytic activity. Considering the versatility of MOF design, IEF-11 could serve as a leading structure for developing a series of Ti-MOFs with visible response by adjusting the Ti-O-Ti connectivity, ligand functionalization and postsynthetic modifications to obtain a new generation of efficient solar MOF photocatalysts.

4. Experimental Section

Reagents and solvents:

All the chemicals were acquired from commercial sources and used as received without further purification.

Synthesis of IEF-11 – $[Ti_2O_3(C_4O_4)]$:

255 mg of finely ground squaric acid (2.24 mmol, Acros Organics 99%) were suspended in 8.2 mL of isopropanol (107.0 mmol, Chem-Lab, >99 wt %) in a 25 mL round-bottom flask, magnetically stirred at 450 rpm for 5 min at room temperature (RT) and sonicated in an ultrasound bath for another 5 min. Then, 6.4 mL of glacial acetic acid (111.9 mmol, J.T. Baker) were added and sonicated again for 15 min. Then, 2.24 mmol of Ti(OBu)$_4$ (762 µL, Acros Organics, >98 wt %) ~~the Ti precursor (662 µL of Ti(iPrO)$_4$, Acros Organics, 98+% or 762 µL of Ti(OBu)$_4$, Acros Organics, >98 wt %)~~ were slowly added to the previous solution

under stirring and then, heated at 50 ºC for 15 min. Note here that the Ti precursor could be replaced Ti(^{i}PrO)$_4$ obtaining similar results but however with slightly lower crystallinity–. Molar ratio Ti/squaric acid/iPrOH/CH_3CO_2H was 1/1/48/50. The resulting orange suspension was transferred into a 23 mL Teflon-lined steel autoclave, sealed and heated at 120 ºC for 48 h with heating and cooling ramps of 1.5 ºC min^{-1}. The resulting orange-brown solid was filtered under vacuum, washed with *i*-PrOH and dried in open air at RT. Yield – 80 wt %

Con formato: Superíndice

General instrumentation:

Laboratory powder X-ray diffraction (PXRD) patterns were collected on a Malvern-Panalytical Empyrean diffractometer fitted with a PIXcel3D Si-strip position-sensitive detector (1D regime was utilized), operating in reflection mode with Ni-filtered Cu $K\alpha_{1,2}$ radiation ($K_{\alpha1}$ = 1.5406 Å, $K_{\alpha2}$ = 1.5444 Å, $K_{\alpha2}/K_{\alpha1}$ = 0.5) at 45 kV and 40 mA. Samples were prepared by placing a thin layer of the appropriate material on a zero-background silicon crystal plate. High resolution powder X-ray diffraction data were collected at CRISTAL beamline, SOLEIL synchrotron facility (Saint-Aubin, France). The sample of IEF-11 was packed into 1.0 mm diameter borosilicate glass capillary (Hilgenberg, no. 50) in open air and sealed with wax. The capillary sample was mounted onto a 2-circle goniometer and spun (100 rpms). The data were collected at RT utilizing the multi-analyzers detector (21-Si(111) crystals). Two independent scans were measured and merged for final analysis. The accurate wavelength (λ = 0.72826 Å) and peak profile parameters were extracted from NIST SRM 660a (LaB_6) peak positions and profile standard data. Fourier transformed infrared (FTIR) spectra were collected in the 4000 to 400 cm^{-1} range using a Thermo Nicolet 6700 FTIR with ATR accessory instrument (Thermo scientific, USA). X-ray photoelectron spectra (XPS) of IEF-11 sample were collected on a SPECS spectrometer with a MCD-9 detector using a monochromatic Al (Kα= 1486.6 eV) X-ray source. The C1s peak at 284.4 eV was used as binding energy reference. Diffuse reflectance UV-Vis and liquid phase UV-Vis measurements

were recorded in a Perkin Elmer (Lambda 19). Elemental analyses were carried out in a Flash 2000 analyzer from Thermo Scientific. Inductively coupled plasma optical emission spectroscopy (ICP-OES) analyses were done in a 2300 DV spectrometer equipment from Perkin Elmer. Thermogravimetric analyses (TGA) were carried out using a SDT Q-600 thermobalance (TA instruments). Variable-temperature powder X-ray diffraction (VTPXRD) data were collected on a D8 Advance Bruker AXS θ–2θ diffractometer ($Cu_{K\alpha}$ radiation, λ=1.54178 Å), equipped with a LYNXEYE XE detector, operating at 40 kV and 40 mA and an Anton Paar XRK 900 high-temperature chamber. Gas sorption experiments were carried out in a Quantachrome Autosorb iQ3 equipment. The dynamic light scattering (DLS) experiments were carried out in a Zetasizer analyzer (Nano Series) from Malvern Panalytical. Scanning electron microscopy (SEM) images were collected in a JEOL JSM-7900F microscope operating between 1 and 2 kV. 3DED data were collected using a JEOL JEM2100 TEM, equipped with a Timepix detector from Amsterdam Scientific Instruments, while continuously rotating the crystal at 0.45° s^{-1}. The data collection was carried out using Instamatic,[50] with an initial unit cell determination being done using REDp.[51] Data reduction was carried out using XDS[52] and the structure of IEF-11 could then be solved from the extracted intensities using SHELXT.[53]

Crystallographic studies:

The structure IEF-11 was refined using TOPAS-Academic V6,[54] using the unit cell and space group acquired from the 3DED data. More precise lattice parameters, peak shapes, and background function were determined by Pawley refinements, leading to the cell of a = 10.51687(9) Å and c = 7.18772(6) Å (R_{wp} = 3.94%, R_p= 3.02%, χ = 1.17). Strong anisotropic size effect broadening required for accurate description of peak profiles and was approximated by spherical harmonics set of parameters symmetrized according to 6/mmm Laue class.[55] For a more physically meaningful description of the anisotropic peak

broadening, due to morphology of the nanoparticles, the approach described by Ectors *et al*.[56] was used. The orthogonal shape of particles by original classification was attributed to biaxial cylinder. The structure model, acquired from 3DED (Figure S2, Table S1), was used as a starting point for a Rietveld refinement (Figure S3, Table S2).

Con formato: Sin Resaltar

Photocatalytic tests

The photocatalytic water splitting experiments were carried out only with water, in the presence of methanol as sacrificial electron donor or in the presence of $Ce(NH_4)_2(NO_3)_6$ as sacrificial electron acceptor. All the experiments were carried out at least in triplicate with a dispersion below 5 %. The presented data corresponds to the average values of the independent experiments. Briefly, the required amount of IEF-11 solid was dispersed in 20 mL of distilled H_2O or a mixture of H_2O (16 mL) and methanol (4 mL) or a solution 0.1 mM of $Ce(NH_4)_2(NO_3)_6$ in water, using a quart reactor (51 mL) and the system sonicated for 20 min to obtain a good solid dispersion. In order to control the reaction temperature, the quart reactor was equipped with a cooling jacket connected to a laboratory chiller. Then, the system was purged with Ar for 1 h. The suspension under 150 rpm magnetic stirring was irradiated with a Hg-Xe lamp (150 W). In other cases, a cut-off filter (λ >455 nm) or an AM 1.5 filter were used to ensure visible light or the simulated sunlight irradiation, respectively.

The evolved gases from all experiments were analyzed taking aliquots at different reaction times. The reaction aliquots were injected into an Agilent 490 Micro GC system (Molsieve 5 Å column using Ar as carrier gas). The temperature of the reactor was monitored and the pressure was analyzed by means of a manometer.

Con formato: Sin Resaltar

Photoinduced electron transfer experiments

Photoinduced electron transfer measurements were carried out using MV^{2+} (20 mg) or $PDA^{+\cdot}$ (20 mg) in a solution of 0.4 mg of MOF/1.75 mL of CH_3CN. The solution was sonicated,

placed in quartz cuvette capped with septum, and purged with Ar for 10 min *prior* irradiation. The cuvettes containing the MOF dispersions under Ar atmosphere were irradiated using a Hg-Xe lamp (150 W) for different times, and the UV-Vis absorbance was measured with a Cary 50 Conc UV-Vis spectrophotometer. The photoinduced electron transfer measurements were followed by the increase of the absorption band centered near 400 nm, corresponding to the $MV^{\cdot+}$ radical cation or the decrease of the absorption band centered near 650 nm, corresponding to the $PDA^{+\cdot}$ radical cation.

Photocurrent measurements

Photocurrent measurements were carried out using an Ag/AgCl as a reference electrode, a Pt electrode as a counter electrode and a transparent fluoride-doped tin oxide (FTO)-coated glass with a thin layer of the corresponding material as a working electrode. *Prior* the measurement, the system was purged with Ar in order to remove the oxygen present in the cell. The photocurrent was measured under dark and under illumination upon polarizing the working electrode at potentials from 1.4 to -0.2 V. Irradiation was performed using an optical fiber connected to a 150 W Hg-Xe lamp.

EPR measurements.

EPR spectra were carried out using a Bruker EMX instrument operating at the X band. Briefly, the IEF-11 solid (3 mg) was suspended into a mixture of acetonitrile-triethanolamine solution (6 mL; v/v 5/1) and the dispersion sonicated for 20 min (450 W). Subsequently, this suspension was divided into two EPR tubes. The EPR spectrum of one of these samples previously purged with Ar for 10 min was recorded at 77 K. The other sample was irradiated with simulated sunlight (150 W, optical fiber equipped with a AM 1.5 filter) for 1 h and its EPR spectrum recorded at 77 K. Subsequently, the temperature of this vial was allowed to reach room temperature, purged with O_2 for 20 min and, then, purged with Ar for 10 min

Con formato: Fuente: Cursiva

Con formato: Fuente: Cursiva

Con formato: Subíndice

before the EPR spectrum is recorded at 77K. Similar measurements were carried out using IEF-11 solid (3 mg) suspended in water (6 mL).

Supporting Information
Supporting Information is available from the Wiley Online Library or from the author.

Acknowledgements

Authors acknowledge the Ramón Areces Foundation project H+MOFs, the M-ERA-NET C-MOF-cell project and Retos Investigación MOFSEIDON (PID2019-104228RB-I00, MICIU-AEI/FEDER, UE) project. S. N. thanks financial support by Ministerio de Ciencia, Innovatión y Universidades RTI2018–099482-A-I00 project and Agència Valenciana de la Innovació (AVI, INNEST/2020/111) project. H. G. thanks financial support to the Spanish Ministry of Science and Innovation (Severo Ochoa and RTI2018-098237-CO21) and Generalitat Valenciana (Prometeo2017/083). T.W. acknowledges financial support from the Swedish Research Council (VR, 2019-05465)

Received: ((will be filled in by the editorial staff))
Revised: ((will be filled in by the editorial staff))
Published online: ((will be filled in by the editorial staff))

References

[1] G. Ferey, *Science* **2005**, *309*, 2040.

[2] H. Furukawa, N. Ko, Y. B. Go, N. Aratani, S. B. Choi, E. Choi, A. O. Yazaydin, R. Q. Snurr, M. O'Keeffe, J. Kim, O. M. Yaghi, *Science* **2010**, *329*, 424.

[3] O. K. Farha, I. Eryazici, N. C. Jeong, B. G. Hauser, C. E. Wilmer, A. A. Sarjeant, R. Q. Snurr, S. T. Nguyen, A. Ö. Yazaydın, J. T. Hupp, *J. Am. Chem. Soc.* **2012**, *134*, 15016.

[4] Themed issues: Metal-organic frameworks, *Chem. Soc. Rev., 2009, 1201; Chem. Rev., 2012, 112; Chem. Soc. Rev., 2014, 5415.*

[5] M. P. Suh, H. J. Park, T. K. Prasad, D.-W. Lim, *Chem. Rev.* **2011**, *112*, 782.

[6] M. R. Ryder, J.-C. Tan, *Mater. Sci. Technol.* **2014**, *30*, 1598.

[7] M. Ding, X. Cai, H.-L. Jiang, *Chem. Sci.* **2019**, *10*, 10209.

[8] J. J. Low, A. I. Benin, P. Jakubczak, J. F. Abrahamian, S. A. Faheem, R. R. Willis, *J.*

Código de campo cambiado

Am. Chem. Soc. **2009**, *131*, 15834.

[9] Y. Gao, M. Zhang, C. Chen, Y. Zhang, Y. Gu, Q. Wang, W. Zhang, Y. Pan, J. Ma, J. Bai, *Chem. Commun.* **2020**, *56*, 11985.

[10] S. Yuan, J. S. Qin, C. T. Lollar, H. C. Zhou, *ACS Cent. Sci.* **2018**, *4*, 440.

[11] Y. Bai, Y. Dou, L.-H. Xie, W. Rutledge, J.-R. Li, H.-C. Zhou, *Chem. Soc. Rev.* **2016**, *45*, 2327.

[12] H. Assi, G. Mouchaham, N. Steunou, T. Devic, C. Serre, *Chem. Soc. Rev.* **2017**, *46*, 3431.

[13] L. Li, X. Wang, T. Liu, J. Ye, *Small Methods* **2020**, *4*, 2000486.

[14] L. Rozes, C. Sanchez, *Chem. Soc. Rev.* **2011**, *40*, 1006.

[15] T. Devic, C. Serre, *Chem. Soc. Rev.* **2014**, *43*, 6097.

[16] S. Remiro-Buenamañana, M. Cabrero-Antonino, M. Martínez-Guanter, M. Álvaro, S. Navalón, H. García, *Appl. Catal. B Environ.* **2019**, *254*, 677.

[17] H. L. Nguyen, T. T. Vu, D. Le, T. L. H. Doan, V. Q. Nguyen, N. T. S. Phan, *ACS Catal.* **2017**, *7*, 338.

[18] J. Castells-Gil, N. M. Padial, N. Almora-Barrios, I. Da Silva, D. Mateo, J. Albero, H. García, C. Martí-Gastaldo, *Chem. Sci.* **2019**, *10*, 4313.

[19] J. Castells-Gil, N. M. Padial, N. Almora-Barrios, J. Albero, A. R. Ruiz-Salvador, J. González-Platas, H. García, C. Martí-Gastaldo, *Angew. Chemie Int. Ed.* **2018**, *57*, 8453.

[20] M. Wen, K. Mori, Y. Kuwahara, T. An, H. Yamashita, *Appl. Catal. B Environ.* **2017**, *218*, 555.

[21] H. Li, Y. Sun, Z.-Y. Yuan, Y.-P. Zhu, T.-Y. Ma, *Angew. Chemie* **2018**, *130*, 3276.

[22] Y. Keum, S. Park, Y.-P. Chen, J. Park, *Angew. Chemie Int. Ed.* **2018**, *57*, 14852.

[23] M. B. Chambers, X. Wang, L. Ellezam, O. Ersen, M. Fontecave, C. Sanchez, L. Rozes, C. Mellot-Draznieks, *J. Am. Chem. Soc.* **2017**, *139*, 8222.

[24] Z. Huang, E. S. Grape, J. Li, A. K. Inge, X. Zou, *Coord. Chem. Rev.* **2021**, *427*, 213583.

[25] F. Gándara, B. Gómez-Lor, M. Iglesias, N. Snejko, E. Gutiérrez-Puebla, A. Monge, *Chem. Commun.* **2009**, 2393.

[26] S. Goswami, A. Adhikary, H. S. Jena, S. Biswas, S. Konar, *Inorg. Chem.* **2013**, *52*, 12064.

[27] P. M. Usov, T. D. Keene, D. M. D'Alessandro, *Aust. J. Chem.* **2013**, *66*, 429.

[28] S. Goswami, H. S. Jena, S. Konar, *Inorg. Chem.* **2014**, *53*, 7071.

[29] R. B. Lin, L. Li, H. L. Zhou, H. Wu, C. He, S. Li, R. Krishna, J. Li, W. Zhou, B. Chen, *Nat. Mater.* **2018**, *17*, 1128.

[30] B. Bueken, H. Reinsch, N. Reimer, I. Stassen, F. Vermoortele, R. Ameloot, N. Stock, C. E. A. Kirschhock, D. De Vos, *Chem. Commun.* **2014**, *50*, 10055.

[31] Z. Abdin, A. Zafaranloo, A. Rafiee, W. Mérida, W. Lipiński, K. R. Khalilpour, *Renew. Sustain. Energy Rev.* **2020**, *120*, 109620.

[32] Y. Shi, A.-F. Yang, C.-S. Cao, B. Zhao, *Coord. Chem. Rev.* **2019**, *390*, 50.

[33] Y. An, B. Xu, Y. Liu, Z. Wang, P. Wang, Y. Dai, X. Qin, X. Zhang, B. Huang, *ChemistryOpen* **2017**, *6*, 701.

[34] P. Salcedo-Abraira, S. M. F. Vilela, A. A. Babaryk, M. Cabrero-Antonino, P. Gregorio, F. Salles, S. Navalón, H. García, P. Horcajada, *Nano Res.* **2021**, *14*, 450.

[35] Y. An, Y. Liu, P. An, J. Dong, B. Xu, Y. Dai, X. Qin, X. Zhang, M.-H. Whangbo, B. Huang, *Angew. Chemie Int. Ed.* **2017**, *56*, 3036.

[36] A. Melillo, M. Cabrero-Antonino, S. Navalón, M. Álvaro, B. Ferrer, H. García, *Appl. Catal. B Environ.* **2020**, *278*, 119345.

[37] M. Cabrero‐Antonino, J. Albero, C. García‐Vallés, M. Álvaro, S. Navalón, H. García, *Chem. – A Eur. J.* **2020**, *26*, 15682.

[38] J. Zhang, T. Bai, H. Huang, M. Yu, X. Fan, Z. Chang, X. Bu, *Adv. Mater.* **2020**, *32*, 2004747.

[39] N. Stock, *Microporous Mesoporous Mater.* **2010**, *129*, 287.

[40] M. A. Halcrow, *Chem. Soc. Rev.* **2013**, *42*, 1784.

[41] D. Zagorac, H. Muller, S. Ruehl, J. Zagorac, S. Rehme, *J. Appl. Crystallogr.* **2019**, *52*, 918.

[42] Y. Peng, A. Rendón-Patiño, A. Franconetti, J. Albero, A. Primo, H. García, *ACS Appl. Energy Mater.* **2020**, *3*, 6623.

[43] S. Song, C. Peng, *J. Dispers. Sci. Technol.* **2005**, *26*, 197.

[44] G. V. Lowry, R. J. Hill, S. Harper, A. F. Rawle, C. O. Hendren, F. Klaessig, U. Nobbmann, P. Sayre, J. Rumble, *Environ. Sci. Nano* **2016**, *3*, 953.

[45] A. Majedi, F. Davar, A. R. Abbasi, *Int. J. Nano Dimens.* **2016**, *7*, 1.

[46] H. Hu, Z. Wang, L. Cao, L. Zeng, C. Zhang, W. Lin, C. Wang, *Nat. Chem.* **2021**, *13*, 358.

[47] D. Mateo, A. Santiago‐Portillo, J. Albero, S. Navalón, M. Alvaro, H. García, *Angew. Chemie Int. Ed.* **2019**, *58*, 17843.

[48] K. G. M. Laurier, E. Fron, P. Atienzar, K. Kennes, H. Garcia, M. Van der Auweraer, D. E. De Vos, J. Hofkens, M. B. J. Roeffaers, *Phys. Chem. Chem. Phys.* **2014**, *16*, 5044.

[49] A. A. Babaryk, O. R. Contreras Almengor, M. Cabrero-Antonino, S. Navalón, H. García, P. Horcajada, *Inorg. Chem.* **2020**, *59*, 3406.

[50] M. O. Cichocka, J. Ångström, B. Wang, X. Zou, S. Smeets, *J. Appl. Crystallogr.* **2018**, *51*, 1652.

[51] W. Wan, J. Sun, J. Su, S. Hovmöller, X. Zou, *J. Appl. Crystallogr.* **2013**, *46*, 1863.

[52] W. Kabsch, *Acta Crystallogr. Sect. D Biol. Crystallogr.* **2010**, *66*, 125.

[53] G. M. Sheldrick, *Acta Crystallogr. Sect. C Struct. Chem.* **2015**, *71*, 3.

[54] A. Coelho, *TOPAS-Academic V6*, Coelho Software, **2016**.

[55] M. Jarvinen, *J. Appl. Crystallogr.* **1993**, *26*, 525.

[56] D. Ectors, F. Goetz-Neunhoeffer, J. Neubauer, *J. Appl. Crystallogr.* **2015**, *48*, 189.